Bubble formation from sub-millimeter orifices: experimental analysis and modeling

Mohseni, E.; Chiamulera, M.; Reinecke, S.; Hampel, U.;

Originally published:

February 2022

Chemical Engineering and Processing: Process Intensification 173(2022), 108809

DOI: https://doi.org/10.1016/j.cep.2022.108809

Perma-Link to Publication Repository of HZDR:

https://www.hzdr.de/publications/Publ-33258

Bubble formation from sub-millimeter orifices: experimental analysis and modeling

E. Mohseni[a,b,*], M. Eduarda Chiamulera[b], S.F. Reinecke[b], U. Hampel[a,b]

[a] *Helmholtz-Zentrum Dresden-Rossendorf, Institute of Fluid Dynamics, Bautzner Landstraße 400, 01328 Dresden, Germany*
[b] *Chair of Imaging Techniques in Energy and Process Engineering, Technische Universität Dresden, Dresden, 01062, Germany*

Abstract

We developed a theoretical model that estimates the bubble size from sub-millimeter orifices under *variable gas flow conditions*. The model is successfully tested for orifices with diameters in the range of 0.2 mm to 1 mm under both quasi-static and dynamic bubbling regimes. The model is able to predict the final bubble radius with an accuracy better than 20% compared with the experimental results. Moreover, we explicitly look into the influence of the gas reservoir volume V_c upstream of the orifice on the gas reservoir pressure P_c by simultaneously monitoring the events, i.e. changes in the state of bubble, upstream and downstream of orifices. We found that, variations in P_c reduce as V_c increases. Analysis of the dynamics of the dominating forces acting on a bubble show that, enlarging V_c mainly amplifies the gas momentum force and the liquid inertia force. Hence, the bubble detachment mechanism may no longer be only buoyancy driven.

Keywords: Bubble formation, Sub-millimeter orifice, Gas reservoir, Bubble dynamics, Modeling

1. Introduction

Gas bubble dispersion is involved in many industrial processes that deal with heat or mass transfer as well as particle separation [1, 2, 3, 4, 5]. In such processes, efficiency strongly depends on the available gas-liquid interfacial area and therefore the bubble size. It is often required to reduce the bubble size in order to enhance process efficiency. This is achievable by scaling down the opening from which bubbles are generated. Accordingly, sub-millimeter orifices are currently of high interest in the industrial sector. Aside from the orifice size, the bubble volume depends on various parameters [6]. Among others, the volume of the gas reservoir V_c upstream of the orifice has a decisive effect on the bubble formation process as it defines the gas flux q through the orifice into the bubble.

The gas feed and the orifice are hydraulically connected via the gas reservoir. For a very small V_c, a high-pressure

*Corresponding author
Email address: ehsan.mohseni@tu-dresden.de (E. Mohseni)
URL: www.hzdr.de (E. Mohseni)

drop develops between the gas feed and the orifice. If the pressure drop is substantially higher than the pressure fluctuations due to the bubble formation, q can be assumed constant. In this case events upstream of the reservoir do not interact with the events at the other end of the reservoir, where bubbles form because of the high flow resistance. This condition is referred to as bubbling under *constant gas flow conditions* CGFC. The latter can be realized by using a long capillary between the orifice and the gas reservoir [7, 8]. On the contrary, when V_c is not negligible, q varies during the bubble formation. This is referred to as the bubbling under *variable gas flow conditions* VGFC. Tadaki [9] defined the criterion at which the transition from CGFC to VGFC occurs using the dimensionless capacitance number:

$$Nc = \frac{4V_c g \rho_l}{\pi d_{or}^2 P_{or}}. \tag{1}$$

Here, P_{or} is the pressure at the orifice plate. According to Tadaki [9], for $Nc > 1$ formation of bubbles occurs under VGFC. In practice, most of the bubble generators operate under VGFC since maintaining such a small V_c that satisfies the requirement of CGFC is not feasible. A further condition can arise when V_c is substantially larger than the generated bubble volumes V_b. In this case, the pressure fluctuations due to gas flux through the orifice results in a minor change in the gas reservoir pressure P_c. This condition is widely recognized as the bubble formation under *constant gas pressure conditions* CGPC and it occurs at $Nc > 9$ [9].

Depending on V_c, V_b can be calculated theoretically if the volumetric gas flow rate to the reservoir Q and the orifice diameter d_{or} are known. For that, several theoretical models are available, which provide information about the bubble dynamics as well as the bubble size during the formation. These models can be broadly classified into spherical and non-spherical models. While non-spherical models require extensive computational effort, spherical models have shown to be accurate in a wide range of operating conditions while being less computationally expensive [10, 11, 12]. Therefore, these models remain thoroughly practical.

A summary of available spherical models for VGFC is given in Table 1. In the table, principal attributes of each model are provided. VGFC models are divided into two categories. In the first category, the gas pressure level in the reservoir is assumed constant and bubbles are generated under CGPC, i.e. $Nc > 9$. In this case, models consider various forces on a bubble and apply the equation of motion to calculate the bubble volume. Detailed expressions of acting forces are provided in Table 2. Hayes et al. [13] were the first to propose a model for CGPC. In their model, the equation of motion is derived for a bubble which, in the first stage undergoes a radial expansion and in the second stage experiences a translational movement. Davidson and Schuler [14] approximated the volumetric gas discharge q

through the orifice from the orifice equation:

$$q = \frac{dV_b}{dt} = K\sqrt{P_c - P_{atm} - \rho_l g h - \frac{4\sigma_{lg}}{d_{or}} + \rho_l g s_b}, \tag{2}$$

where, K is an orifice constant. In Equation (2), the effects of liquid viscosity and liquid kinetic energy are neglected. Moreover, the viscous drag force is also excluded from the equation of motion of the bubble. Satyanarayan et al. [15] used the same approach and calculated the bubble volume within two stages. They calculated q from Equation (2). However, they considered a constant gas flow rate for the second stage with a value calculated at the end of the first stage.

In the second category of VGFC models, q and P_c are assumed variable. In this case, different approaches are proposed to account for the change in q. While Khurana and Kumar [16] used an electrical analogy to obtain q, Swope [17] used a modified average volumetric gas flow rate Q entering the gas reservoir. Swope [17] multiplied Q to the ratio of the bubbling time t_b over the sum of t_b and the waiting time t_w. Park et al. [18] applied a material balance in the gas reservoir and the ideal gas law for an adiabatic condition to correlate P_c and V_c. Subsequently, the bubble volume V_b is calculated since the gas flow rate is equal to the change of V_b.

More recent VGFC models use the application of the potential flow theory to account for the liquid flow velocity surrounding a bubble. This theoretical approach was first used by McCann and Prince [19]. They modeled the motion of a bubble which experiences a radial expansion and translational motion through an unbounded surrounding liquid. In this case, the velocity potential ϕ can be described as follows:

$$\phi = \phi_T + \phi_E = \frac{r_b^3}{2r^2}\left(\frac{ds_b}{dt}\right)\cos\delta + \frac{r_b^2}{r}\left(\frac{dr_b}{dt}\right). \tag{3}$$

Here, r is the length of an imaginary line between a given point in the liquid and the center of the bubble, and δ is the angle between this line and a virtual line perpendicular to the orifice plate. Subsequently, the pressure in the liquid phase is calculated via the unsteady form of Bernoulli's equation:

$$\frac{P_l}{\rho_l} = \frac{\partial\phi}{\partial t} - \frac{U_l^2}{2} - g s_b + \frac{P_{or}}{\rho_l}. \tag{4}$$

In a similar approach, Kupferberg and Jameson [20] considered the effect of the adjacent orifice wall. To account for the influence of the adjacent wall, the method of images from Lamb [21] is adopted in the potential function:

$$\begin{aligned}\phi = {} & \frac{ds_b}{dt}\left[\frac{r_b^3}{2r^2} + \frac{rr_b^3}{8s_b^3} + \frac{r_b^6}{16s_b^3 r^2} + \frac{rr_b^6}{64s_b^6} + \frac{r_b^9}{128s_b^6 r^2} + \cdots\right]\cos\delta + \\ & \frac{dr_b}{dt}\left[\frac{r_b^2}{r} + \left(\frac{rr_b^2}{4s_b^2} + \frac{r_b^5}{8s_b^2 r^2} + \frac{rr_b^5}{32s_b^5} + \frac{r_b^8}{64s_b^5 r^2} + \cdots\right)\cos\delta\right].\end{aligned} \tag{5}$$

By substituting Equation (5) into Equation (4), it is possible to calculate the liquid pressure at the bubble interface. Accordingly, the bubble pressure can be calculated using a pressure jump at the interface due to the effect of surface tension. Moreover, q is calculated using the law of conservation of mass and the first law of thermodynamics. Eventually, a system of ordinary differential equations is solved to calculate V_b.

McCann and Prince [19] included the effect of liquid inertia due to the bubble translational motion. They also considered the wake effect from the preceding bubble. Kupferberg and Jameson [20] proposed a criterion for liquid weeping into the orifice. Tsuge and Hibino [22] considered an empirical coefficient to incorporate the effect of liquid viscosity. Dias [23] accounted for the influence of the gas kinetic energy which was neglected in the model proposed by Kupferberg and Jameson [20]. Zhang and Tan [24] used Oseen's modification to the potential flow theory to provide a more realistic prediction of the wake pressure of the preceding bubble. Later on, they proposed a model including the effect of liquid phase cross-flow [25]. Ruzicka et al. [26] used the mass balance and the Hagen–Poiseuille equation to calculate the gas flow rate into the bubble. Besides, they used the Rayleigh-Plesset equation to relate the change of bubble size to the pressure change in the reservoir and the bubble.

According to Table 1, sub-millimeter orifices have not been considered in any models under VGFC. This limitation is believed to be due to V_c. According to Equation 1, V_c is directly proportional to the squared d_{or}. Therefore, by changing the orifice size from the millimeter range to the sub-millimeter range under VGFC, V_c has to be significantly reduced. In this context, we provide a model based on the prior works of Kupferberg and Jameson [20] and Dias [23] with certain modifications. The model is presented in Section 2 and later it is validated experimentally. The experimental setup is presented in Section 3. Aside from the model, we had a close look at the simultaneous developments of pressure variations in the gas reservoir and the bubble interface at different levels of V_c. Moreover, the leverage of various forces acting on a bubble under VGFC are discussed. These parameters, as well as the validation of the model, are presented in Section 4.

Table 1: Spherical models for bubble formation under variable gas flow conditions VGFC.

Reference	Method	$d_{or}\,(mm)$	$Eö$	$We \times 10^3$	Nc	Detachment criterion
Hayes et al. [13]	equation of motion	0.79-6.35	0.08-2.04	1-35	4-261	exp. observation
Davidson and Schuler [14]	orifice equation and equation of motion	0.52, 0.64	0.05-0.08	0-31	$(1.6\text{-}2.5) \times 10^4$	$s_b = r_b + r_{or}$
Satyanarayan et al. [15]	orifice equation and equation of motion	0.51-4	0.04-5.29	4.1-86	293-18046	$s_b = r_b + r_{or}$
Potter [27]	force balance, equation of motion			No validation		$l_n = r_{or}$
Khurana and Kumar [16]	force balance, equation of motion	2.7	1.72	0.16-2.48	0.9-10	$s_b = r_b + r_{or}$
McCann and Prince [19]	Bernoulli equation, orifice equation, potential flow theory	4.76-9.52	3-12.1	0.47-136.8	2.9-150	$s_b = r_b$
Kupferberg and Jameson [20]	force balance, orifice equation, potential flow theory	3.17-6.35	1.35-5.41	0.02-21.78	0.06-60	$s_b = r_b + r_{or}$
Swope [17]	orifice equation	1.345	0.24	$(0.05\text{-}0.28) \times 10^{-3}$	3.5	analytical solution
Park et al. [18]	material balance, application of ideal gas law	1.21-3.3	0.13-7.18	0-0.09	0.09-84	$\Delta P_c = 4\sigma_{lg}/d_{or}$
Tsuge and Hibino [22]	orifice equation, modified potential flow theory	1.08-2.12	0.16-0.81	0-7.47	1-75	$l_n = d_{or}$
Dias [23]	mass and energy balance, orifice equation, potential flow theory	3.2	1.39	6×10^{-5}	5	$s_b = 1.55 r_b$
Zhang and Tan [24]	mass and energy balance, orifice equation, potential flow theory	3.2-9.6	1.39-12.55	< 93	1.4-26	$s_b = r_b$
Zhang and Tan [25]	mass and energy balance, orifice equation, potential flow theory	4.8-6.4	3.14-6.4	0.41-0.98	25-45	$s_b = r_b + (1 - 0.02U_l)d_{or}$
Ruzicka et al. [26]	mass balance, orifice equation, Rayleigh-Plesset equation, equation of motion	1.6	0.35	$(0.14\text{-}1.55) \times 10^{-2}$	17	$s_b = r_b + d_{or}$

Table 2: Detailed expression for the forces acting on a bubble.

Forces	Expressions	Direction	Units
Buoyancy force	$F_B = g(\rho_l - \rho_g)V_b - \rho_l g h \pi r_d^2$	Upward	$[m.\frac{N}{m}]$
Pressure force	$F_P = \left(\frac{2\sigma_{lg}}{r_b} + \rho_g g h\right)\pi r_d^2$	Upward	$[m^2.\frac{N}{m^2}]$
Gas momentum force	$F_M = \rho_g \frac{q^2}{\pi r_{or}^2}$	Upward	$[\frac{kg}{m^3}\frac{m}{s}\frac{m^2}{s}]$
Surface tension force	$F_S = 2\pi\sigma_{lg} r_d \sin\vartheta$	Downward	$[\frac{N}{m}.m]$
Drag force	$F_D = \frac{1}{2}\rho_l C_D A_b U_b^2$	Downward	$[m^2.\frac{N}{m^2}]$
Liquid inertia force	$F_{LI} = \left(\frac{11}{16}\rho_l + \rho_g\right)\left[V_b\frac{dU_b}{dt} + U_b\frac{dV_b}{dt}\right]$	Downward	$[\frac{kg}{m^3}.\frac{m^4}{s^2}]$

2. Modeling

The new model solves the bubble volume in two consecutive stages: the expansion stage and the elongation stage. In the former stage, the bubble grows in the radial direction while it remains attached to the orifice. Hence, the axial elevation of the bubble in this stage is due to the radial expansion. The termination of this stage occurs when the forces acting on the bubble are at equilibrium. During the elongation stage, the bubble undergoes a translational motion while it radially expands as well. The termination of this stage is defined based on the detachment criterion proposed by Mohseni et al. [28]. The model bases on the following assumptions:

- The bubble remains spherical throughout the formation process except at the bubble base, which can freely expand on the orifice surface.
- The equilibrium contact angle remains constant throughout the formation process.
- The submergence level of the orifice is much larger than the size of the bubble and the wall effect is negligible.
- The gas phase is assumed to be ideal and obeying an adiabatic equation of state.
- The liquid phase is assumed inviscid, irrotational and incompressible.
- The wake of the leading bubble does not affect the formation of the bubble.

A schematic of the stages of the model is illustrated in Figure 1.

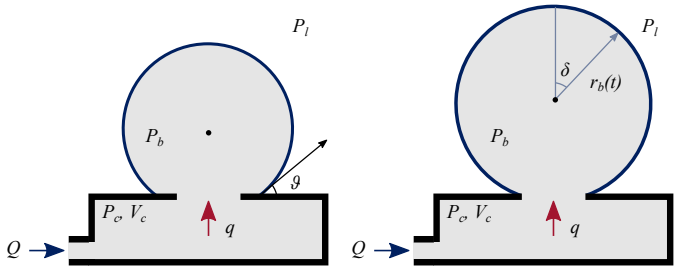

Figure 1: Schematic of the expansion stage (left) and the elongation stage (right) of a bubble in the model.

Change in the reservoir pressure due to the discharge of the gas through the orifice can be expressed using the continuity equation and the equation of state of an ideal gas. Considering a control volume CV enclosed in a control surface CS for the gas reservoir, the continuity equation can be written as follows:

$$\int_{\mathrm{CS}} \rho_g \vec{U} \cdot \hat{n} dS + \int_{\mathrm{CV}} \frac{\partial \rho_g}{\partial t} dV_c = 0. \tag{6}$$

Here, $\vec{U}$ is fluid velocity and $\hat{n}$ is the unit exterior normal to the CS. Assuming that gas enters the reservoir at the inlet and exits from the orifice, and assuming that the density and the pressure of gas are uniformly distributed in the reservoir at all times, Equation (6) becomes:

$$-\rho_g U_i S_i + \rho_g U_{or} S_{or} + \frac{d\rho_g}{dt} V_c = 0. \tag{7}$$

Here, S_i and S_{or} are the cross-sectional area of reservoir inlet and outlet, respectively. The equation of state of a perfect gas in the reservoir can be written as follows:

$$P_c = \frac{\rho_g c^2}{\gamma}. \tag{8}$$

Here, c is the speed of sound in the perfect gas and γ is the heat capacity ratio of the gas ($\gamma = C_p/C_v$). Since c and γ can be assumed constant, Equation (8) can be written as follows:

$$\frac{d\rho_g}{dt} = \frac{\gamma}{c^2}\frac{dp}{dt} \tag{9}$$

By inserting Equation (9) in Equation (7), we arrive at the following:

$$P_c - (P_c)_{t=0} = -\frac{c^2 \rho_g}{\gamma V_c}\left[V_b - (V_b)_{t=0} - Qt\right]. \tag{10}$$

Here, $t = 0$ indicates the initial condition of the corresponding parameter.

A mass balance for an imaginary control volume limited by the gas reservoir cross-section S_c and the outer cross-section of the orifice S_{or} yields:

$$U_c = U_{or}\frac{S_{or}\rho_{or}}{S_c \rho_c}. \tag{11}$$

It is assumed that the gas in the orifice is incompressible. For the highest gas flow rate through the smallest orifice in our experiments, the Mach number Ma did not exceed 0.09. This is far below $Ma = 0.3$ beyond which the compressiblity effects of the fluid becomes important [29]. Hence, the assumption of incompressibility of the gas in the orifice seems to be adequate. Therefore, the gas density in the orifice ρ_{or} is equal to ρ_c. Moreover, assuming the flow of gas to be isentropic, steady, and irrotational, the macroscopic energy balance for the aforementioned imaginary control volume leads to the Bernoulli's equation:

$$P_c + \frac{1}{2}\rho_c U_c^2 = P_{or} + \frac{1}{2}\rho_{or} U_{or}^2. \tag{12}$$

The above correlation describes the relationship between the pressure in the gas reservoir P_c and the orifice P_{or}. Assuming that the latter is equal to the bubble pressure P_b and substituting Equation (11) in Equation (12), q can be

calculated as follows:

$$q = C_d S_{or} \sqrt{\frac{2\left(P_c - P_b\right)}{\rho_c \left[1 - \left(\frac{S_{or}}{S_c}\right)^2\right]}}. \tag{13}$$

Here, C_d is the orifice discharge coefficient which accounts for the jet-contraction (*vena contracta*) and non-uniformity of gas flow velocity across the orifice. The orifice discharge coefficient is calculated according to the ratio of the orifice cross-section to the gas reservoir cross-section β and the Reynolds number of the gas flowing in the reservoir $Re_c = \rho_g d_c U_c / \mu_g$ as follows:

$$C_d = 0.5959 + 0.0312\beta^{2.1} - 0.184\beta^8 + \frac{91.71\beta^{2.5}}{Re_c}. \tag{14}$$

According to the experimental values, the orifice discharge coefficient usually lays within the range 0.6 and 0.62 [30, 31].

Since the liquid flow field around the bubble is assumed to be inviscid and irrotational, the potential flow solution can be applied. For the case in hand, the influence of the orifice wall is considered and the zero normal velocity at the wall is satisfied. Accordingly, the wall effect can be simulated using the potential flow solution for the fluid around two equisized spheres, which simultaneously expand and move away from each other along the same axis. This is represented by Equation (5) given $s_b \geq r_b$. Hence, it can only be used from the termination of the expansion stage. The liquid pressure around the bubble can be described using the unsteady form of Bernoulli's equation:

$$\frac{P_l}{\rho_l} = \frac{\partial \phi}{\partial t} - \frac{U_l^2}{2} - g(s_b + r\cos\delta) + \frac{P_{or}}{\rho_l}, \tag{15}$$

where $P_{or} = P_{atm} + \rho_l g h$ and,

$$U_l^2 = \left(\frac{\partial \phi}{\partial r}\right)^2 + \left(\frac{1}{r}\frac{\partial \phi}{\partial \delta}\right)^2. \tag{16}$$

By using the the potential function provided in Equation (5), the liquid pressure at the bubble interface P_{int} at $r = r_b$ can be calculated as follows:

$$P_{int} = P_{atm} + \rho_l g h + \rho_l \left[\left(r_b \frac{d^2 r_b}{dt^2}\right) + \frac{3}{2}\left(\frac{dr_b}{dt}\right)^2 - g s_b + \Gamma_1 \cos\delta + \Gamma_2 \cos^2\delta + \Gamma_3 \sin^2\delta\right]. \tag{17}$$

The coefficients Γ_1, Γ_2, and Γ_3 are provided in Appendix A. Subsequently, the bubble pressure is $P_b = P_{int} + 2\sigma_{lg}/r_b$ by considering the surface tension pressure. As mentioned earlier, it is assumed that the bubble maintains a spherical shape. The pressure gradients travel with the speed of sound within the bubble. Hence, the bubble pressure can be taken constant, and yet it is independent of δ. Hence, the term with $\cos\delta$ in Equation (15) can be disregarded. The

final equation for the bubble expansion stage can be obtained by substituting for P_c and P_b from Equations (10) and modified (17) in Equation (13) as follows:

$$\frac{d^2 r_b}{dt^2} = g\frac{s_b}{r_b} - \frac{3}{2r_b}\left(\frac{dr_b}{dt}\right)^2 - \frac{c^2\rho_g}{r_b\gamma V_c\rho_l}\left[V_b - (V_b)_{t=0} - Qt\right] - \frac{\rho_g\left(\frac{dV_b}{dt}\right)^2}{\rho_l r_b C_d^2 S_{or}^2} + \frac{2\sigma_{lg}}{r_b\rho_l}\left(\frac{1}{(r_b)_{t=0}} - \frac{1}{r_b}\right). \tag{18}$$

The system of equations is numerically solved to calculate r_b, $\frac{dr_b}{dt}$, and time t_{ex} at the end of the expansion stage using the standard Runge-Kutta fourth-order scheme given the following initial conditions:

$$(r_b)_{t=0} = \frac{d_{or}}{2\sin\vartheta}, \tag{19}$$

$$\left(\frac{dr_b}{dt}\right)_{t=0} = 0, \tag{20}$$

$$(P_c)_{t=0} = P_{atm} + \rho_l g h + \frac{2\sigma_{lg}}{(r_b)_{t=0}}, \tag{21}$$

$$(P_b)_{t=0} = P_{atm} + \rho_l g h + \frac{2\sigma_{lg}}{(r_b)_{t=0}}. \tag{22}$$

In the experimental setup, the ratio of the diameter of the orifice to the one from the gas reservoir is less than 0.03. Hence, the ratio of S_{or}/S_c in Equation (13) is assumed to be negligible. In the presented model, the bubble base expansion is enabled, hence the bubble instantaneous volume can be calculated as follows:

$$V_b = \frac{4}{3}\pi r_b^3 - \frac{1}{3}\pi r_b^3(1-\cos\vartheta)^2(2+\cos\vartheta). \tag{23}$$

The expansion stage concludes when the sum of all forces on the bubble is equal to zero. This criterion is satisfied when the integration of the liquid force on the bubble interface in the vertical direction from Equation (17) is zero and $s_b = r_b\cos\vartheta$:

$$\int_0^{\pi}(2\pi P_{int} r^2\sin\delta\cos\delta)_{r=r_b} = 0. \tag{24}$$

The mathematical derivation of Equation (24) is provided in Appendix B. During the elongation stage, the bubble acceleration is neglected. The bubble, however, has a radial expansion and translational motion. Therefore, the condition $s_b = r_b\cos\vartheta$ no longer holds and the system of equations needs to account for an additional correlation regarding

the unknown s_b. This is obtained by substituting for P_{int} in Equation (24) from Equation (17):

$$\frac{d^2 s_b}{dt^2} = \left[\left(g - \left[\frac{3}{8}\left(\frac{r_b}{s_b}\right)^2 + \frac{3}{64}\left(\frac{r_b}{s_b}\right)^5\right]\frac{d^2 r_b}{dt^2}\right) - \left(\frac{1}{r_b}\left[\frac{3}{8}\left(\frac{r_b}{s_b}\right)^2 + \frac{9}{8}\left(\frac{r_b}{s_b}\right)^5\right]\left(\frac{dr_b}{dt}\right)^2\right) + \left(\frac{1}{r_b}\left[\frac{9}{16}\left(\frac{r_b}{s_b}\right)^4 + \frac{9}{64}\left(\frac{r_b}{s_b}\right)^7\right]\left(\frac{ds_b}{dt}\right)^2\right) - \left(\frac{1}{r_b}\left[\frac{3}{2} - \frac{9}{128}\left(\frac{r_b}{s_b}\right)^6\right]\left(\frac{dr_b}{dt}\right)\left(\frac{ds_b}{dt}\right)\right)\right] \left(\frac{1}{2} + \frac{3}{16}\left(\frac{r_b}{s_b}\right)^3 + \frac{3}{128}\left(\frac{r_b}{s_b}\right)^6\right)^{-1}. \tag{25}$$

Here again, the system of equations is solved using the standard Runge-Kutta fourth order method with following initial conditions:

$$(r_b)_{t_{el}=0} = r_e, \tag{26}$$

$$\left(\frac{dr_b}{dt}\right)_{t_{el}=0} = \left(\frac{dr_b}{dt}\right)_{t=t_{ex}}, \tag{27}$$

$$(s_b)_{t_{el}=0} = r_e \cos\vartheta, \tag{28}$$

$$\left(\frac{ds_b}{dt}\right)_{t_{el}=0} = \left(\frac{dr_b}{dt}\right)_{t=t_{ex}}. \tag{29}$$

The elongation stage terminates using the detachment criterion proposed by Mohseni et al. [28]. This criterion relates the non-spherical geometry of a bubble prior to the detachment to its equivalent spherical shape. The criterion is as follows:

$$\frac{s_b}{d_{or}} = D_1\left(\frac{d_b}{d_{or}}\right)^{D_2} + D_3. \tag{30}$$

Here, coefficients D_1 to D_3 are as follows:

$$D_1 = 0.2453,\ D_2 = 1.279,\ D_3 = 1.485. \tag{31}$$

3. Experimental methods

A detailed description of the experimental setup is given in Mohseni et al. [28]. Hence, only necessary information is provided here. Table 3 provides the specifications of both phases. A bubble column made of acrylic glass with dimensions ($80\times80\times1000$ mm^3) was filled up to 800 mm with deionized water. Local bubble rising induced liquid velocity in the column is suppressed using three wire-mesh baffles at 100 mm above the orifice plate with 150 mm spacing be-

tween the baffles. Stainless-steel circular orifice plates with 0.5 mm thickness and roughness of $R_Z = 1 \pm 0.03$ µm are mounted on a gas reservoir. Each plate contains a single perforation in the middle. The volume of the gas reservoir is accurately adjusted using a precision linear-stage with less than 25 µm positioning error in 100 mm displacement. The dynamic pressure fluctuations in the gas reservoir are monitored using a sensitive microphone, model 106B52 from series 106B microphones of PCB Group, Inc. The resolution of the sensor is 1.3 µbar and a response time of 12.5 µs. The signal of the dynamic pressure sensor was recorded synchronously to the camera by a transient data recorder, LTT24 from Labortechnik Tasler GmbH, at a sample rate of 1 MHz. Consequently, the changes in the reservoir pressure were tracked simultaneously to the bubble growth.

Table 3: Characteristics of the continuous phase and the dispersed phase.

Medium	$\kappa\,(\frac{\mu S}{cm})$	$\rho\,(\frac{\mathrm{kg}}{\mathrm{m}^3})$	$\mu\,(\frac{\mathrm{kg}}{\mathrm{ms}})$	$T\,(^\circ\mathrm{C})$
Deionized water	34.1	998.2	8.9×10^{-4}	25
Air	3×10^{-11}	1.184	1.84×10^{-5}	25

Table 4 provides information regarding the range of experiments. The surface tension coefficient and the apparent contact angle were measured at 0.072 N/m and $74^\circ \pm 0.7$, respectively. For each orifice, two gas flow rates corresponding to the quasi-static bubbling regime and the dynamic bubbling regime are studied [8]. The transition from the quasi-static regime to the dynamic regime is indicated by the critical volumetric gas flow rates Q_c as follows [32]:

$$Q_c = \pi \left(\frac{16}{3g^2}\right)^{\frac{1}{6}} \left(\frac{\sigma_{lg} d_{or}}{2\rho_l}\right)^{\frac{5}{6}}. \tag{32}$$

Accordingly, the normalized rates of $Q/Q_c = 0.5$ and $Q/Q_c = 1.5$ were fed to each orifice to generate bubbles under the quasi-static regime and the dynamic regime, respectively. The influence of V_c can be represented by the capacitance number Nc. Previous studies defined the range $1 < Nc < 10$ in which the influence of V_c should be considered [33, 16]. However, this range is mostly validated for millimeter-sized orifices. In the current investigation, a wide range of $0.2 \leq Nc \leq 50$ is covered within two sets of experiments. The first set of experiments covers a comparable range of Nc as previous investigations. Accordingly, the influence V_c on the bubble formation is studied at constant gas flow rates of $Q/Q_c = 0.5$ and $Q/Q_c = 1.5$ in a range of $0.2 < Nc < 15$ for all orifices. The corresponding measurement matrix is provided in Figure 2 (left). In the second set of experiments, the range of Nc is extended for the orifices smaller than 0.5 mm up to $Nc = 50$, see Figure 2 (right). The gas flow rate for this set of measurements is kept constant at $Q/Q_c = 0.5$. To investigate the bubble dynamics, videometry with a back-light technique is utilized. The processing of the images is done using a proprietary image processing algorithm developed by Ziegenhein [34]. Detailed explanation of the optical measurement technique as well as the image processing method are explained in

Mohseni et al. [28].

Table 4: Characteristics and operating conditions at various orifices operating under VGFC.

ID	d_{or} (µm)	Q ($\frac{\text{SmL}}{\text{min}}$)	Q_c ($\frac{\text{SmL}}{\text{min}}$)	$E\ddot{o}$ ($\times 10^{-3}$)	We ($\times 10^{3}$)	Nc
O-200	207	9.95 , 29.8	19.9	5.770	0.22 , 1.94	0.2 ⋯ 50
O-300	315	14.1 , 42.3	28.2	13.32	0.11 , 1.11	0.2 ⋯ 50
O-400	412	17.6 , 52.8	35.3	22.82	0.08 , 0.77	0.2 ⋯ 50
O-500	488	20.3 , 60.9	40.6	32.01	0.07 , 0.62	0.2 ⋯ 50
O-600	614	24.5 , 73.6	49.0	50.30	0.05 , 0.44	0.2 ⋯ 15
O-700	699	27.4 , 82.2	54.8	65.59	0.04 , 0.38	0.2 ⋯ 15
O-800	788	30.3 , 90.8	60.5	83.31	0.04 , 0.32	0.2 ⋯ 15
O-900	887	33.4 , 100	66.8	105.7	0.03 , 0.28	0.2 ⋯ 15
O-1000	993	36.7 , 110	73.4	132.3	0.03 , 0.24	0.2 ⋯ 10

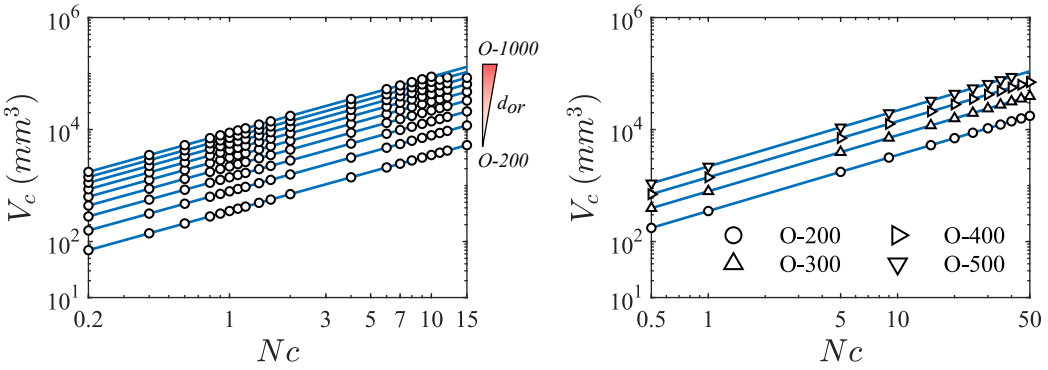

Figure 2: Data points for the investigations on bubble formation under VGFC, up to $Nc = 15$ (left) and up to $Nc = 50$ (right).

4. Results and discussion

4.1. Pressure variations in the gas reservoir

Pressure variations in the gas reservoir ΔP_c are explained using the exemplary orifice O-300 operating at a low gas flow rate $Q/Q_c = 0.5$ with small, medium, and large values of V_c. Figure 3 shows development of ΔP_c in a small V_c for three consecutive bubbles. In this case, after bubble detachment, the gas-liquid interface enters into the orifice. Due to the liquid weeping, V_c reduces. The latter, along with simultaneous gas feed into the reservoir Q, results in a sharp increase in ΔP_c up to the point (I) in Figure 3. From this point, ΔP_c linearly increases, although the gas-liquid interface is still inside the orifice. Tracking the curvature of the bubble-cap from point (II) to point (III) suggests that, the radius of the bubble-cap within this period remains constant, see Figure 4. This radius is equal to the orifice radius and it is known as the critical radius. Considering the similar trend of the pressure evolution before and after point (II), one can assume that the critical radius is already achieved at point (I). From this point, the gas pocket is rising

through the orifice. There is no simple explanation for the behavior of the gas-liquid interface for the period before point (I). However, the influence of the liquid weeping and consequently the effect of the liquid inertia and the liquid viscosity in such a small gas reservoir is believed to be highly relevant.

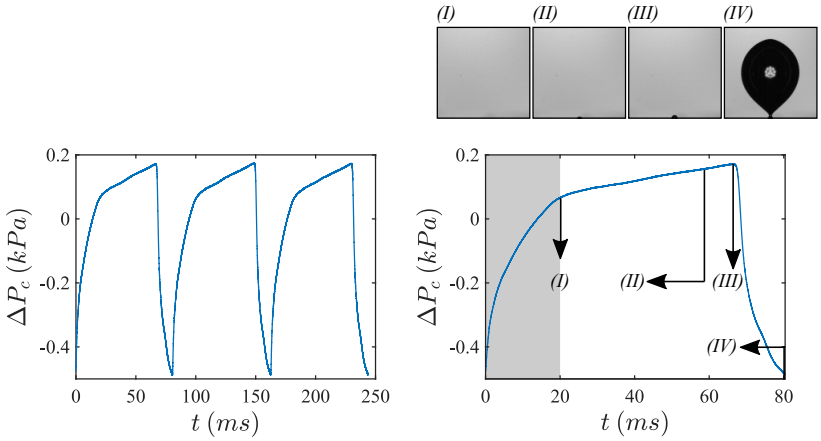

Figure 3: Pressure evolution in the gas reservoir for three consecutive cycles (left) and the first cycle only (right) of bubble formation from *O*-300 at $Q/Q_c = 0.5$ with $V_c = 0.003\,cm^3$ and $Nc = 0.5$.

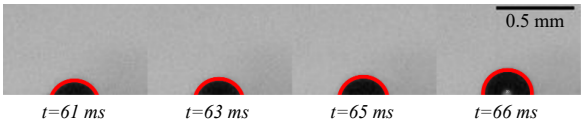

Figure 4: Evolution of the bubble-cap prior to the spontaneous growth, $t = 61$ ms and $t = 66$ ms refer to the points (II) and (III) in Figure 3, respectively.

By increasing V_c, the range of ΔP_c reduces. The value of ΔP_c in the case of the bubble in Figure 5 is 0.15 kPa, compared to 0.65 kPa in the case of the bubble in Figure 3. Liquid weeping also occurs in this case, although no sharp increase in ΔP_c can be observed after the departure of the leading bubble. In comparison to the case with smaller V_c, the duration of the formation cycle is almost half and ΔP_c decreases linearly during the gas discharge to the bubble.

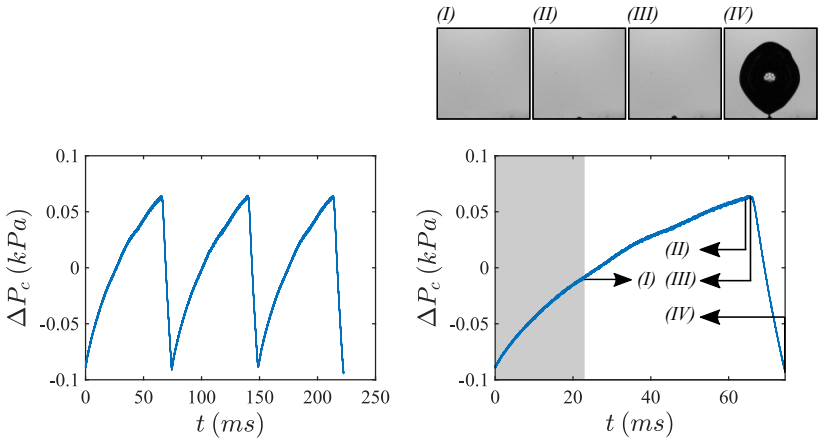

Figure 5: Pressure evolution in the gas reservoir for three consecutive cycles (left) and the first cycle only (right) of bubble formation from *O*-300 at $Q/Q_c = 0.5$ with $V_c = 11.8\,cm^3$ and $Nc = 15$.

By further increasing V_c, ΔP_c decreases even more. In this case, the volumetric gas discharge into the bubble q becomes so high that it causes a change in the bubbling regime. However, even with a new bubbling regime, the maximum ΔP_c remains lower than for smaller reservoirs. As it can be seen in Figure 6, ΔP_c drops quickly in the course of spontaneous bubble formation. The first bubble is generated within less than 10 ms, Figure 6 point (II). Subsequently, the secondary bubble grows and reaches out to the leading bubble. The growth of the secondary bubble is believed to be due to the high gas kinetic energy during the discharge process, re-establishment of a spherical gas pocket after the bubble detachment, and the influence of the wake of the leading bubble by establishing a low-pressure area above the secondary bubble.

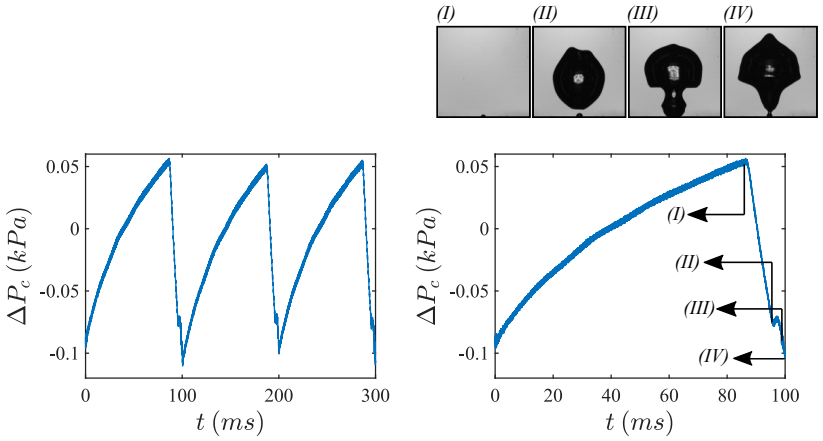

Figure 6: Pressure evolution in the gas reservoir for three consecutive cycles (left) and the first cycle only (right) of bubble formation from *O*-300 at $Q/Q_c = 0.5$ with $V_c = 15.77\,cm^3$ and $Nc = 20$.

Figure 7 shows the trend of maximum pressure variations in the reservoir $\Delta P_{c,max}$ with regard to V_c and therefore Nc. In this figure, $\Delta P_{c,max}$ is normalized using the capillary pressure of the orifice $P_{cap} = 4\sigma_{lg}/d_{or}$. According to

Equation 22 and for a similar experimental conditions, the minimum required P_c for formation of bubbles from various orifices depends only on P_{cap} and consequently d_{or}. Hence, $\Delta P_{c,max}/P_{cap}$ in Figure 7 not only indicates the trend of maximum pressure variations but also its portion with regard to d_{or}. In general, $\Delta P_{c,max}$ reduces as Nc increases. By increasing Nc, $\Delta P_{c,max}$ initially remains constant or slightly increases and reaches to a maximum. From this point onward, the influence of V_c becomes important. For O-200, the maximum $\Delta P_{c,max}$ is only about 20% of P_{cap} and the influence of V_c can be seen even with the smallest reservoirs. However, $Nc \geq 20$, $\Delta P_{c,max}$ seems to be independent of Nc for O-200. In the case of O-300, $\Delta P_{c,max}$ initially increases, which is due to the increase in the size of generated bubbles, and then it gradually reduces to about $Nc = 11$. At this point, $\Delta P_{c,max}$ increases again which is due to the change in the regime of bubbling from single bubbling to double bubbling. For orifices larger than O-300, the magnitude of $\Delta P_{c,max}$ due to the bubble formation increases. Moreover, the trend of the evolution of $\Delta P_{c,max}$ by increasing Nc becomes similar among the orifices. However, the local maximums of $\Delta P_{c,max}$ occurs at slightly different Nc.

Above observations suggest that, for sub-millimeter orifices the range of Nc within which the influence of V_c on bubble formation should be considered, varies with the orifice size. In other words, VGFC can be achieved in different ranges of Nc for sub-millimeter orifices. This is in contrary to observations from millimeter orifices where the lowest and the highest limits of VGFC reported to be $Nc = 1$ and $Nc = 10$, respectively [9, 18]. Moreover, $\Delta P_{c,max}$ is directly related to the size of the orifice d_{or}, the rate of volumetric gas flow Q, the size of the gas reservoir V_c, and consequently the diameter of bubbles d_b generated from the orifice. Hence, to interpret the behavior of $\Delta P_{c,max}$, the influence of these parameters should be considered simultaneously.

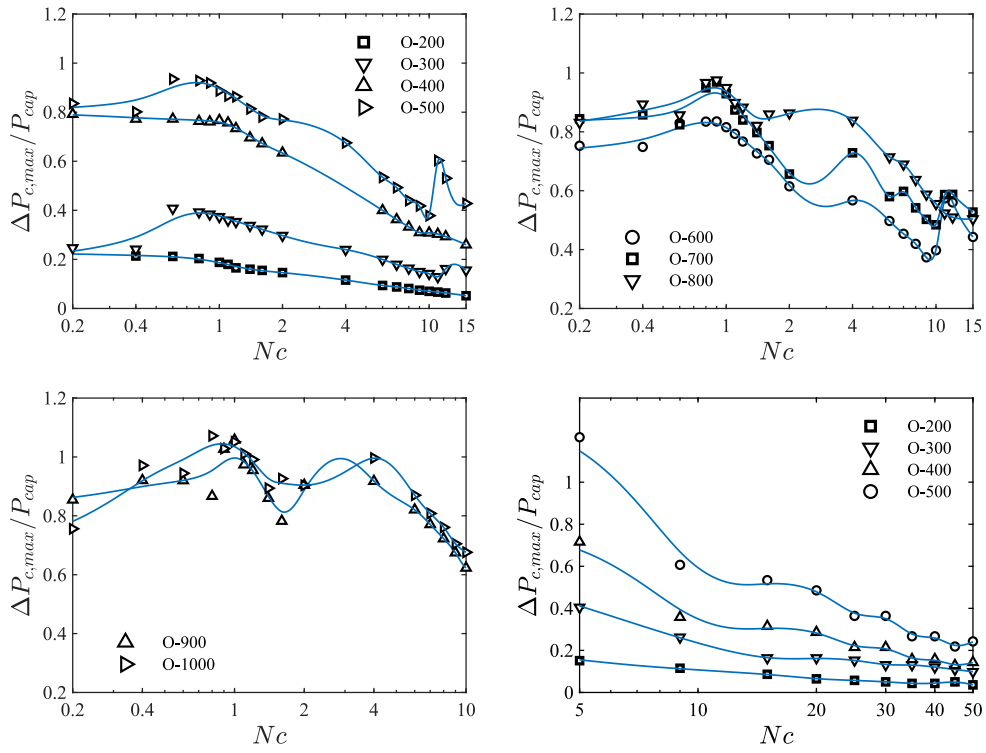

Figure 7: Pressure variation in the gas reservoir due to bubble formation at $Q/Q_c = 0.5$ at various capacitance numbers.

4.2. Forces acting on a bubble

Figure 8 illustrates the typical evolution of the acting forces on the bubble during the formation from O-1000 and O-600 at $Q/Q_c = 0.5$. The magnitude of individual forces is calculated from the expressions provided in Table 2. In the calculation of forces, the influence of the dynamic apparent contact angle ϑ and the bubble base expansion are included. In the case of orifices in Figure 8, the dominant forces are respectively the buoyancy force F_B and the liquid inertia force F_{LI} in upward and downward directions. Moreover, depending on the size of the gas reservoir V_c, the gas momentum force F_M and the surface tension force F_S can be relatively important. For the bubble generators with a small V_c corresponding to $Nc = 0.2$, F_S remains important throughout the formation of the bubble, except shortly after the beginning of the formation. As the bubble starts to expand, the apparent contact angle temporarily reduces to nearly zero. Hence, the magnitude of F_S reduces accordingly. By increasing V_c, the duration in which the apparent contact angle ϑ is negligible prolongs toward the later stage of the formation. Hence, the contribution of F_S on the formation process becomes less important. The magnitude of F_{LI} increases with V_c. It is previously explained that one of the circumstances of increasing V_c is the generation of larger bubbles. This increase in the bubble volume is a result of the excessive q, which in turn amplifies F_M and consequently enhances F_{LI}. The latter is related to the velocity and acceleration of the bubble, see Table 2. For the given range of orifices and gas flow rates, the influence of the drag

force F_D is negligible. Similarly, the influence of the pressure force F_P is insignificant except at the very beginning of the formation process.

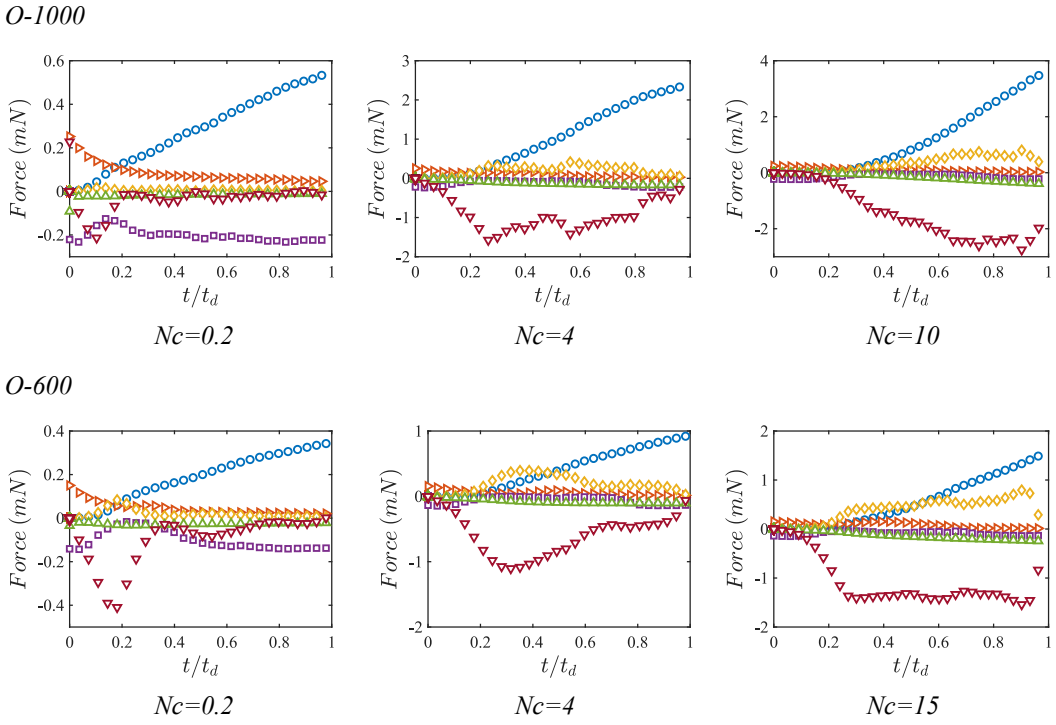

Figure 8: Typical evolution of forces acting on a growing bubble for O-1000 and O-600 at $Q/Q_c = 0.5$ with various gas reservoir sizes (legend: ○ F_B ▷ F_P ◇ F_M □ F_S △ F_D ▽ F_{LI}).

By reducing d_{or}, the influence of the gas kinetic energy becomes more important. Hence, F_M acts effectively and pushes the bubble in the axial direction. On the contrary, the F_{LI} resists this bubble elongation and becomes the only dominant downward force during the formation. As it can be seen in Figure 9, both F_{LI} and F_M grow in magnitude as Nc increases. On the upward direction and by increasing Nc or reducing d_{or}, F_M takes over F_B and becomes the dominant upward force. Moreover, by reducing d_{or}, the influence of F_P becomes stronger as a result of the formation of smaller bubbles. Similar to the larger orifices, the contribution of F_D is negligible regardless of the size of the orifice.

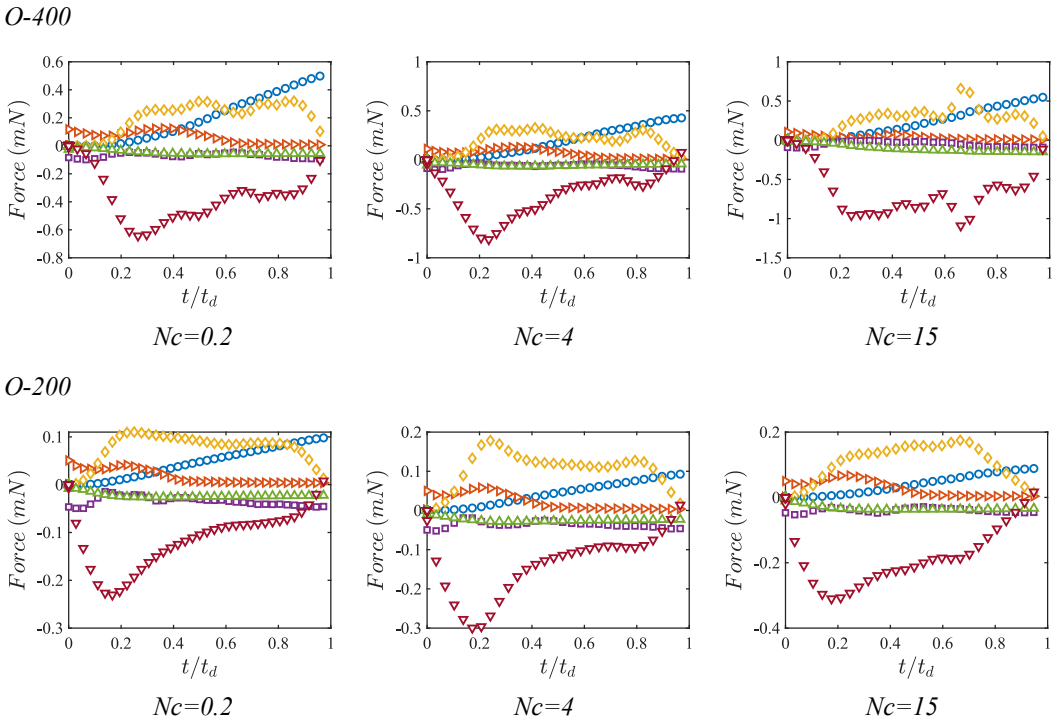

Figure 9: Evolution of forces acting on a growing bubble for *O*-400 and *O*-200 at $Q/Q_c = 0.5$ with various gas reservoir sizes (legend: ○ F_B ▷ F_P ◇ F_M □ F_S △ F_D ▽ F_{LI}).

4.3. Model validation

The presented model solves the bubble volume from a spherical submerged orifice with a diameter in the range of $0.2 < d_{or} < 1$ mm in the range of $0.5 \leq Q/Q_c \leq 1.5$ under VGFC. The model is limited to the prediction of the bubble size that is resulted from a single detachment from the orifice. As V_c can alter the bubbling regime, the limit of the presented model, is in the range of $1 \leq Nc \leq 10$. Figure 10 compares the solution of the model with the experimental data from various orifices and volumetric gas flow rates. As it can be seen, the increasing trend of r_b/r_{or} with Nc from the model agrees with experimental results. Moreover, the agreement remains consistent when the normalized gas flow rate Q/Q_c is tripled.

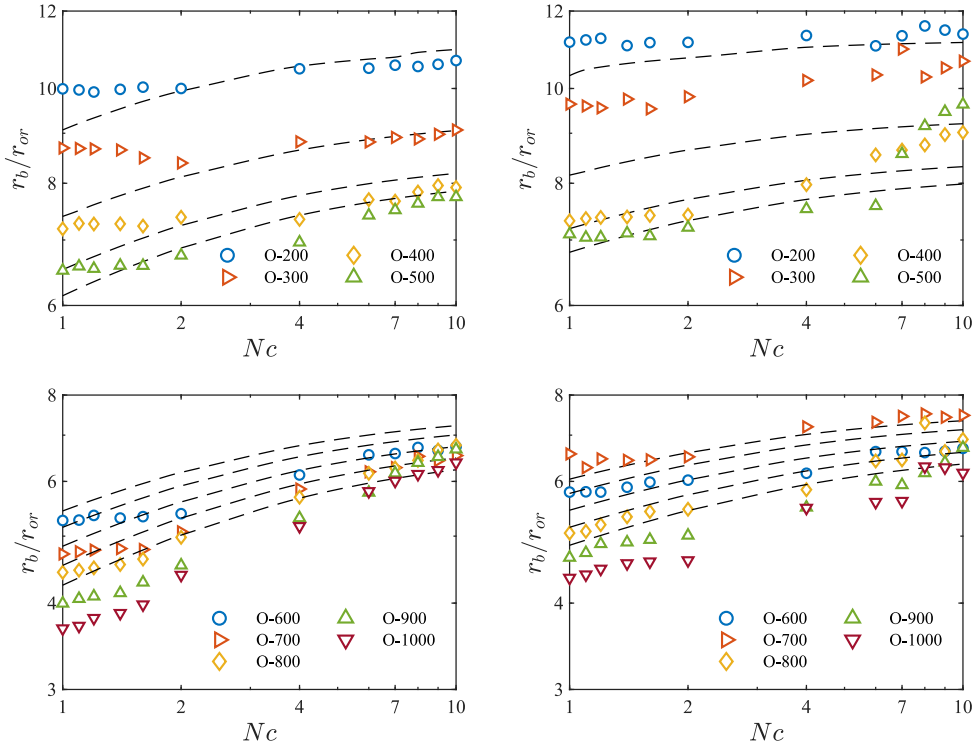

Figure 10: Comparison between the solution of the model (dashed-lines) and experimental data (scattered points) for various orifices at $Q/Q_c \leq 0.5$ (left) and $0.5 \leq Q/Q_c \leq 1.5$ (right).

175 The model predicts the final bubble radius with an accuracy better than 20% compared with the experimental results. Figure 11 reports on the deviation of the solution of the model from experimental data. Accordingly, Figure 11 (left) compares the cumulative data from all the studied orifices in the range of the model validation, $0.5 \leq Q/Q_c \leq 1.5$. Figure 11 (right) depicts the averaged relative error and standard deviation calculated based on the solution of the model and experimental data.

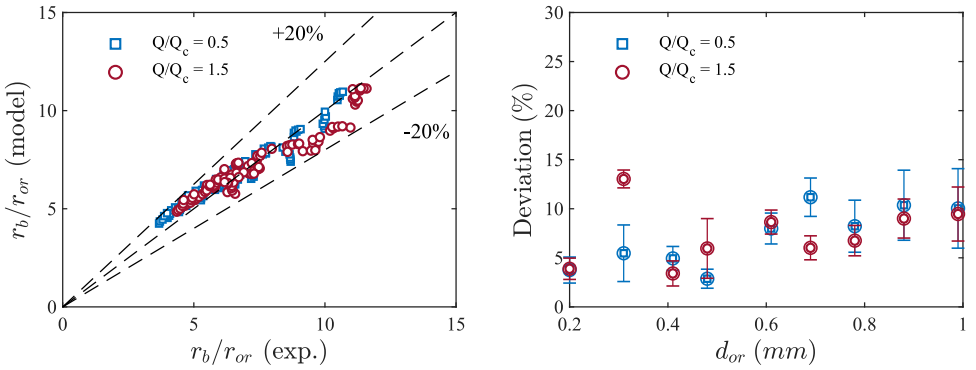

Figure 11: Parity plot of the model prediction and experimental bubble radius (left), and deviation between the model predictions and experimental data for different orifice sizes (right).

5. Conclusion

We studied the formation of bubbles from sub-millimeter orifices submerged in deionized water under VGFC. Accordingly, we conducted a study on influential parameters, namely the orifice diameter d_{or}, the volume of the gas reservoir V_c, and pressure attributes in the reservoir P_c. Moreover, we developed a theoretical model that accurately estimates the bubble size from sub-millimeter orifices under VGFC. A summary of the main findings is as follows:

- For sub-millimeter orifices and during the formation of a bubble, enlarging V_c results in formation of larger bubbles. In this case, as V_c increases, q progressively increases during the formation process.
- The range of variation of the dynamic pressure in the gas reservoir due to the bubble formation reduces as V_c increases.
- Analysis of various forces acting on a bubble during its formation indicates a decisive influence of V_c on the arrangement of dominant forces on the bubble. Increasing V_c enhances q, which in turn amplifies the gas momentum force and the liquid inertia force. For $d_{or} < 0.4$ mm, however, q is dominated by d_{or} and it is less influenced by V_c.
- The presented model predicts the detachment bubble volume from a sub-millimeter submerged orifice under VGFC. Compared to the earlier models, the model includes the influence of the apparent contact angle and the expansion of the bubble base. Moreover, the model uses a new detachment criterion which correlates the non-spherical bubble shape from the experiments to the spherical bubble volumes calculated from the theoretical model. Incorporating these parameters yields an accurate estimation of the bubble volume within the validation range of the present study.

Clearly, V_c has a substantial effect on the bubble size from single sub-millimeter orifices. For the future works, it is suggested to characterize the effect of this parameter in the case of adjacent orifices that are hydraulically connected via the same reservoir. Moreover, the effect of the gas pressure fluctuation on the bubble formation worth investigating.

Acknowledgment

This work is partly funded by the European Social Fund and the Free State of Saxony, reference number: 100284305 and the Initiative and Networking Fund of the Helmholtz Association in the frame of the Clean Water Technology Lab CLEWATEC- a Helmholtz Innovation Lab.

Appendix A. Coefficients in Equation (17)

The detailed description of the coefficients in Equation (17) are given below. As the distance of the bubble's center of mass to the orifice plate is equal or more than the bubble radius, the terms smaller than r_b^7/s_b^7 are neglected.

$$\Gamma_1 = r_b\frac{d^2r_b}{dt^2}\left[\frac{3\,r_b^2}{8\,s_b^2}+\frac{3\,r_b^5}{64\,s_b^5}\right]+r_b\frac{d^2s_b}{dt^2}\left[\frac{1}{2}+\frac{3\,r_b^3}{16\,s_b^3}+\frac{3\,r_b^6}{128\,s_b^6}\right]+\left(\frac{dr_b}{dt}\right)^2\left[\frac{3\,r_b^2}{8\,s_b^2}+\frac{9\,r_b^5}{8\,s_b^5}\right]- \left(\frac{ds_b}{dt}\right)^2\left[\frac{9\,r_b^4}{16\,s_b^4}+\frac{9\,r_b^7}{64\,s_b^7}\right]+\frac{dr_b}{dt}\frac{ds_b}{dt}\left[\frac{3}{2}-\frac{9\,r_b^6}{128\,s_b^6}\right]-gr_b, \tag{A.1}$$

$$\Gamma_2 = \frac{1}{2}\left(\frac{ds_b}{dt}\right)^2, \tag{A.2}$$

$$\Gamma_3 = -\left(\frac{ds_b}{dt}\right)^2\left[\frac{5}{8}+\frac{9\,r_b^3}{32\,s_b^3}+\frac{6.75\,r_b^6}{128\,s_b^6}\right]-\left(\frac{dr_b}{dt}\right)^2\left[\frac{g\,r_b^4}{128\,s_b^4}+\frac{2.25\,r_b^7}{128\,s_b^7}\right]-\frac{dr_b}{dt}\frac{ds_b}{dt}\left[\frac{9\,r_b^2}{16\,s_b^2}+\frac{9\,r_b^5}{63\,s_b^5}\right]. \tag{A.3}$$

Appendix B. Termination of the expansion stage

Mathematical derivation of Equation (24) is provided here. By substituting P_{int} in Equation (24) using Equation (17) and expanding the integral, Equation (24) can be written as follows:

$$\int_0^\pi 2\pi r_b^2\sin\delta\cos\delta\left[p_{atm}+\rho_l gh+\rho_l\left[\left(r_b\frac{d^2r_b}{dt^2}\right)+\frac{3}{2}\left(\frac{dr_b}{dt}\right)^2-gs_b\right]\right]d\delta+ \int_0^\pi 2\pi r_b^2\Gamma_1\rho_l\sin\delta\cos^2\delta d\delta+\int_0^\pi 2\pi r_b^2\Gamma_2\rho_l\sin\delta\cos^3\delta d\delta+\int_0^\pi 2\pi r_b^2\Gamma_3\rho_l\sin^3\delta\cos\delta d\delta=0. \tag{B.1}$$

In the above equation, only the second term on the left hand side of the equation has a non-zero value equal to $\frac{2}{3}$. Hence, to satisfy Equation (B.1), Γ_1 has to be zero. Moreover, at the end of the expansion stage $s_b = r_b\cos\vartheta$, $\frac{ds_b}{dt} = \frac{dr_b}{dt}\cos\vartheta$, and $\frac{d^2s_b}{dt^2} = \frac{d^2r_b}{dt^2}\cos\vartheta$. Hence, the condition for termination of the expansion stage is expressed as follows:

$$(\Gamma_1)_{r=r_b} = r_b\frac{d^2r_b}{dt^2}\left[\left(\frac{3}{8}\cos^2\vartheta+\frac{3}{64}\cos^5\vartheta\right)+\left(\frac{1}{2}+\frac{3}{16}\cos^3\vartheta+\frac{3}{128}\cos^6\vartheta\right)\right](1+\cos\vartheta)+ \left(\frac{dr_b}{dt}\right)^2\left[\left(\frac{3}{8}\cos^2\vartheta+\frac{9}{8}\cos^5\vartheta\right)-\left(\frac{9}{16}\cos^4\vartheta+\frac{9}{64}\cos^7\vartheta\right)+ \left(\frac{3}{2}-\frac{9}{128}\cos^6\vartheta\right)\right](1+\cos\vartheta+\cos^2\vartheta)-gr_b\cos\vartheta=0. \tag{B.2}$$

Nomenclature

Dimensionless groups

Ma	Mach number, $(= U/c)$
Nc	capacitance number, $(= 4V_c\rho_l/\pi d_{or}^2 P_{or})$
Re_c	gas Reynolds number in the reservoir, $(= \rho_g d_c U_c/\mu_g)$

Latin symbols

A	bubble surface area, m^2
A_b	cross-sectional area of bubble, m^2
c	sound velocity, $\frac{\mathrm{m}}{\mathrm{s}}$
C_d	orifice discharge coefficient
C_D	drag coefficient
C_P	heat capacity at constant pressure
C_V	heat capacity at constant volume
d_b	bubble diameter, m
d_c	gas reservoir diameter, m
d_{or}	orifice diameter, m
d_{32}	Sauter mean diameter, m
f	bubble formation frequency, $\frac{1}{\mathrm{s}}$
F	force, N
f^*	quasi-static bubble formation frequency, $\frac{1}{\mathrm{s}}$
g	gravitational acceleration, $\frac{\mathrm{m}^2}{\mathrm{s}}$
h	submergence depth, m
K	orifice constant
l_n	length of the bubble neck, m
P_{atm}	atmospheric pressure, Pa

	P_b	pressure inside a bubble, Pa
	P_c	pressure in gas reservoir, Pa
	P_{cap}	capillary pressure, Pa
	P_{crt}	critical pressure in gas reservoir, Pa
	P_{int}	pressure at the bubble interface, Pa
	P_l	pressure in liquid phase, Pa
	P_{or}	pressure at the orifice plate, Pa
	q	volumetric gas flow rate through orifice, $\frac{m^3}{s}$
	Q	volumetric gas flow rate into the gas reservoir, $\frac{m^3}{s}$
	Q_c	critical volumetric gas flow rate, $\frac{m^3}{s}$
	r_b	bubble radius, m
	r_d	bubble base radius, m
	r_e	bubble radius at the end of radial expansion stage, m
	r_{or}	orifice radius, m
	R_Z	arithmetic average roughness, m
	S	cross-sectional area, m^2
	s_b	distance from bubble's center of mass to the orifice plate, m
	S_c	cross-sectional area of gas reservoir, m^2
	S_i	cross-sectional area of gas reservoir inlet, m^2
	S_{or}	cross-sectional area of orifice, m^2
	t	time, s
	t_b	bubbling time, s
	t_d	bubbling detachment time, s
	t_{ex}	time of the expansion stage, s
	t_{el}	time of the elongation stage, s
	t_w	waiting time, s

	T	absolute temperature, $^{\circ}$K
	U	gas velocity, $\frac{\mathrm{m}}{\mathrm{s}}$
	U_b	bubble rising velocity, $\frac{\mathrm{m}}{\mathrm{s}}$
	U_c	average gas bulk velocity in the reservoir, $\frac{\mathrm{m}}{\mathrm{s}}$
	U_i	average gas velocity entering the reservoir, $\frac{\mathrm{m}}{\mathrm{s}}$
	U_l	liquid velocity, $\frac{\mathrm{m}}{\mathrm{s}}$
	U_{or}	average gas velocity through orifice, $\frac{\mathrm{m}}{\mathrm{s}}$
	V_b	bubble volume, m^3
	V_c	volume of gas reservoir, m^3

Greek symbols

	β	ratio of the orifice cross-section to reservoir cross-section
	γ	specific heat ratio
	δ	angle in Figure 1, $^{\circ}$
	θ	contact angle, $^{\circ}$
	κ	electrical conductivity, $\frac{\mathrm{S}}{\mathrm{m}}$
	μ_l	liquid dynamic viscosity, Pa.s
	μ_g	gas dynamic viscosity, Pa.s
	ρ_c	gas density in the reservoir, $\frac{\mathrm{kg}}{\mathrm{m}^3}$
	ρ_l	density of liquid, $\frac{\mathrm{kg}}{\mathrm{m}^3}$
	ρ_g	density of gas, $\frac{\mathrm{kg}}{\mathrm{m}^3}$
	ρ_{or}	density of gas through orifice, $\frac{\mathrm{kg}}{\mathrm{m}^3}$
	σ_{lg}	liquid-gas surface tension, $\frac{\mathrm{N}}{\mathrm{m}}$
	ϕ	potential function, $\frac{\mathrm{m}^2}{\mathrm{s}}$
	ϕ_E	potential function of expanding bubble, $\frac{\mathrm{m}^2}{\mathrm{s}}$
	ϕ_T	potential function of translating bubble, $\frac{\mathrm{m}^2}{\mathrm{s}}$

References

[1] S. J. Y. Lee, H. An, P. C. Wang, J. G. Hang, S. C. M. Yu, Effects of liquid viscosity on bubble formation characteristics in a typical membrane bioreactor, International Communications in Heat and Mass Transfer (2020) 105000.

[2] P. Painmanakul, K. Loubiere, G. Hebrard, P. Buffière, Study of different membrane spargers used in waste water treatment: characterisation and performance, Chemical Engineering and Processing: Process Intensification 43 (11) (2004) 1347–1359.

[3] Y. T. Kang, T. Nagano, T. Kashiwagi, Visualization of bubble behavior and bubble diameter correlation for nh3–h2o bubble absorption, International journal of refrigeration 25 (1) (2002) 127–135.

[4] R. Lau, R. Mo, W. S. B. Sim, Bubble characteristics in shallow bubble column reactors, Chemical Engineering Research and Design 88 (2) (2010) 197–203.

[5] C. Ribeiro Jr, P. Lage, Experimental study on bubble size distributions in a direct-contact evaporator, Brazilian journal of chemical engineering 21 (1) (2004) 69–81.

[6] A. A. Kulkarni, J. B. Joshi, Bubble formation and bubble rise velocity in gas- liquid systems: a review, Industrial & Engineering Chemistry Research 44 (16) (2005) 5873–5931.

[7] A. Wraith, Two stage bubble growth at a submerged plate orifice, Chemical Engineering Science 26 (10) (1971) 1659–1671.

[8] E. Mohseni, R. Herrmann-Heber, S. Reinecke, U. Hampel, Bubble generation by micro-orifices with application on activated sludge wastewater treatment, Chemical Engineering and Processing-Process Intensification 143 (2019) 107511.

[9] T. Tadaki, The size of bubbles from single orifices, Kagaku Kogaku Ronbunshu 27 (1963) 147–155.

[10] A. Marmur, E. Rubin, A theoretical model for bubble formation at an orifice submerged in an inviscid liquid, Chemical Engineering Science 31 (6) (1976) 453–463.

[11] W. Pinczewski, The formation and growth of bubbles at a submerged orifice, Chemical Engineering Science 36 (2) (1981) 405–411.

[12] H. Tsuge, Y. Nakajima, K. Terasaka, Behavior of bubbles formed from a submerged orifice under high system pressure, Chemical engineering science 47 (13-14) (1992) 3273–3280.

[13] W. Hayes III, B. W. Hardy, C. D. Holland, Formation of gas bubbles at submerged orifices, AIChE Journal 5 (3) (1959) 319–324.

[14] J. Davidson, Bubble formation at an orifice in an inviscid liquid, Transactions of the Institution of Chemical Engineers 38 (1960) 335–342.

[15] A. Satyanarayan, R. Kumar, N. Kuloor, Studies in bubble formation—ii bubble formation under constant pressure conditions, Chemical Engineering Science 24 (4) (1969) 749–761.

[16] A. Khurana, R. Kumar, Studies in bubble formation?iii, Chemical Engineering Science 24 (11) (1969) 1711–1723.

[17] R. D. Swope, Single bubble formation at orifices submerged in viscous liquids, The Canadian Journal of Chemical Engineering 49 (2) (1971) 169–174.

[18] Y. Park, A. L. Tyler, N. de Nevers, The chamber orifice interaction in the formation of bubbles, Chemical Engineering Science 32 (8) (1977) 907–916.

[19] D. J. McCann, R. Prince, Bubble formation and weeping at a submerged orifice, Chemical Engineering Science 24 (5) (1969) 801–814.

[20] A. Kupferberg, Bubble formation at a submerged orifice above a gas chamber of finite volume, Trans. Int. Chem. Engrs. 47 (1969) 241–250.

[21] H. Lamb, Hydrodynamics, Cambridge university press, 1993.

[22] H. TSUGE, S.-I. HIBINO, Bubble formation from an orifice submerged in liquids, Chemical Engineering Communications 22 (1-2) (1983) 63–79.

[23] M. Pereira Dias, Bubble formation at a multiple orifice plate submerged in quiescent liquid (1999).

[24] W. Zhang, R. Tan, A model for bubble formation and weeping at a submerged orifice, Chemical engineering science 55 (24) (2000) 6243–6250.

[25] W. Zhang, R. Tan, A model for bubble formation and weeping at a submerged orifice with liquid cross-flow, Chemical engineering science 58 (2) (2003) 287–295.

[26] M. Ruzicka, M. Vecer, S. Orvalho, J. Drahoš, Effect of surfactant on homogeneous regime stability in bubble column, Chemical Engineering Science 63 (4) (2008) 951–967.

[27] O. Potter, Bubble formation under constant-pressure conditions, Chemical Engineering Science 24 (11) (1969) 1733–1734.

[28] E. Mohseni, T. Ziegenhein, S. Reinecke, U. Hampel, Bubble formation from sub-millimeter orifices under variable gas flow conditions, Chemical Engineering Science 242 (2021) 116698.

[29] F. M. White, Fluid mechanics, Tata McGraw-Hill Education, 1979.

[30] J. H. Perry, Chemical engineers' handbook (1950).

[31] P. J. Pritchard, R. W. Fox, A. T. McDonald, Introduction to fluid mechanics, John Wiley & Sons, 2010.

[32] H. N. Oguz, A. Prosperetti, Dynamics of bubble growth and detachment from a needle, Journal of Fluid Mechanics 257 (1993) 111–145.

[33] O. S. Gokhale, M. A. Jog, R. M. Manglik, Experimental study of chamber volume effect on bubble formation from orifice plates submerged in water, in: ASME International Mechanical Engineering Congress and Exposition, Vol. 52101, American Society of Mechanical Engineers, 2018, p. V007T09A013.

[34] T. Ziegenhein, Fluid dynamics of bubbly flows, PhD Thesis (2016).